The CyberKnife® Robotic Radiosurgery System in 2010

www.tcrt.org

W. Kilby M.Sc.*
J. R. Dooley, Ph.D.
G. Kuduvalli, Ph.D.
S. Sayeh, M.S.
C. R. Maurer Jr., Ph.D.

Accuray Incorporated, 1310 Chesapeake Terrace, Sunnyvale, CA 94089, USA

This review provides a complete technical description of the CyberKnife® VSI™ System, the latest addition to the CyberKnife product family, which was released in September 2009. This review updates the previous technical reviews of the original system version published in the late 1990s. Technical developments over the last decade have impacted virtually every aspect of the CyberKnife System. These developments have increased the geometric accuracy of the system and have enhanced the dosimetric accuracy and quality of treatment, with advanced inverse treatment planning algorithms, rapid Monte Carlo dose calculation, and post-processing tools that allow trade-offs between treatment efficiency and dosimetric quality to be explored. This review provides a system overview with detailed descriptions of key subsystems. A detailed review of studies of geometric accuracy is also included, reporting a wide range of experiments involving phantom tests and patient data. Finally, the relationship between technical developments and the greatly increased range of clinical applications they have allowed is reviewed briefly.

Key words: CyberKnife System; Radiosurgery; Stereotactic Body Radiation Therapy

Introduction

The CyberKnife® Robotic Radiosurgery System (Accuray Incorporated, Sunnyvale, CA, USA) has undergone almost twenty years of technical development from its conception (1) to its most recent version, the CyberKnife VSI™ System, the first of which was installed in April 2010. The CyberKnife System, as described in a series of technical papers in the late 1990s (2-7), began as a *frameless* alternative to existing stereotactic radiosurgery systems such as the Gamma Knife (Elekta AB, Stockholm, Sweden) and conventional linear accelerators (LINACs) equipped with head frames and stereotactic beam collimators. In the original CyberKnife configuration, a LINAC mounted on a robotic manipulator delivered many independently targeted (non-isocentric) and non-coplanar treatment beams with high precision under continual X-ray image guidance. This basic concept remains unchanged, but significant improvements and additions to the system technology implemented in the last decade have made the early technical publications obsolete (Table I and Figure 1), and more recent reviews have either provided limited technical detail (8, 9), or focused principally on commissioning and quality assurance (10, 11). The most recent complete technical system overview was published outside the peer-reviewed literature (12), and described the CyberKnife System version that was current in 2008 (version 8.0), which was subsequently updated in 2009 (version 8.5) and 2010 (CyberKnife VSI System, which uses system version 9.0) to include new functionality. This review provides a complete technical description of the CyberKnife VSI System as it is comprised in 2010.

The technologies described in this review are employed every day by clinicians worldwide to treat brain (13-17), spine (18-23), lung (24-28), prostate (29-32),

*Corresponding Author:
W. Kilby M.Sc.
E-mail: wkilby@accuray.com

Table I

Contrast between the major technical and clinical features of the CyberKnife System in the late 1990's and in 2010 (* indicates current tolerance levels stated in the vendor's equipment specification, ** number of patients treated as of May 1997 (2) *** cumulative number of patients treated at 200 installed systems as of June 2010).

	CyberKnife System in 1997-1999 (2-7)	CyberKnife VSI System in 2010
Image registration and tracking methods	Skull skeletal tracking with 3D translation corrections	1. Skull skeletal tracking with 6D translation and rotation corrections 2. Spine skeletal tracking with 6D corrections 3. Fiducial marker tracking with 6D corrections 4. Lung tumor tracking based on tumor: lung radiographic contrast with 3D corrections 5. Real-time respiratory motion tracking, which can be combined with methods 3 and 4 above
Robotic manipulator precision	0.5 mm	0.12 mm
Overall targeting accuracy (static target)	Mean: 1.6 mm Range: 0.6 mm – 2.5 mm	Maximum: ≤ 0.95 mm*
Overall targeting accuracy (target undergoing respiratory motion)	n/a	Maximum: ≤ 1.5 mm*
Beam Collimation	Fixed circular collimators	Variable aperture circular collimator or fixed circular collimators
Dose-rate	300 MU/min	1000 MU/min
Image detectors	Gadolinium oxysulfide fluoroscopes with pixel size 1.25 x 1.25 mm	Amorphous silicon flat panel detectors with pixel size 0.4 x 0.4 mm
Dose calculation algorithm(s)	Ray Tracing	1. Monte-Carlo 2. Ray Tracing
Robot path traversal	Robot moves through all nodes	Robot moves through nodes selected during treatment planning
Patient positioning system	Manually operated treatment couch	1. Fully integrated 5-DOF standard treatment couch 2. Fully integrated 6-DOF RoboCouch Patient Positioning System (option) 3. Fully integrated 7-DOF RoboCouch with seated load (option)
Clinical applications	Intracranial and upper spine radio-surgery (under FDA Investigational Device Exemption)	Anywhere in the body where radiosurgery is clinically indicated (with FDA 510(k) regulatory clearance). Common treatment sites include intracranial, head & neck, spine & paraspinal, lung, prostate, liver, pancreas. In addition conventionally fractioned Robotic IMRT® is available.
Total patients treated to date	30**	90,000***

liver (33-35), head and neck (36-40) and other extracranial sites (41, 42). This review is intended to provide both clinicians and researchers with the most recent technical details on the complete system; thus, all major system components are described in some detail. Because geometric treatment delivery accuracy is critical to radiosurgery, this review also provides a detailed summary of studies of system accuracy. Finally, we briefly review the relationship between technical and clinical developments that have taken place over the last decade.

Treatment Procedure Overview

Treatment Planning

Treatment planning begins with obtaining one or more three-dimensional (3D) images that allows the target volume and nearby organs at risk (OARs) to be visualized. Once acquired the 3D images are transferred to the MultiPlan® Treatment Planning System (TPS) via a dedicated database server. The minimum requirement is for a volumetric CT study, from which a 3D patient model is generated and within which treatment beams are positioned. Each beam is described by a vector

linking a source point and a direction point. In principle, an infinite number of both source and direction points can be achieved with the delivery system. In practice, the beam geometry is constrained to a practical size during treatment planning using a finite set of candidate beams. The source point is the position of the LINAC focal spot. The direction point is usually within the target volume defined by the user using the imaging datasets. Each source point is a *node* and the complete set of nodes is a *path set*. Different path sets are constructed to provide a range of non-coplanar beam directions for intra- and extra-cranial treatment sites (Figure 2). All non-coplanar beam directions are achieved without moving the patient. The appropriate path set for each patient is selected manually at the start of the treatment planning process. The number of nodes in the different path sets ranges from 23 to 133.

Direction points are determined automatically based on the beam generation mode, which is either isocentric or non-isocentric. The isocentric mode allows the user to position one or more pseudo-isocenters within the patient model resulting in one candidate beam from each node to each pseudo-isocenter. The non-isocentric mode takes advantage of the

Figure 1: The CyberKnife System of (**A**) the late 1990's and (**B-D**) 2010. Panel (**A**) shows the first generation of stand–mounted, flat-panel image detectors (not the fluoroscopes featured in the earliest systems described in Table 1). The most obvious changes between the two systems shown are the robotic manipulator, the positions of the X-ray image detectors, the couch design, and the addition of the boom-mounted stereo camera and the Xchange Robotic Collimator Changer table. Alterations in the LINAC design are not obvious because of the covers. The couch included in (**B**) is the optional RoboCouch Patient Positioning System, which is shown in its seated load configuration in (**C**). The Xchange system table, which is obscured behind the robotic manipulator in (**B**), is shown in more detail in (**D**).

ability of the robotic manipulator to direct each beam at a unique point within the patient, without any need to reposition the patient between beams, by generating a large number of direction points (typically 1,000–6,000) semi-randomly within the target volume and distributes these uniformly among the nodes to form the candidate beam set. The user can choose to prevent candidate beams from passing through OARs, which can be a method to minimize the dose delivered to small radiosensitive structures such as the lens of the eye or the thyroid gland. The user then selects between one and three fixed collimator sizes, or between one and twelve Iris Collimator field sizes, which are assigned to subsets of the candidate beam set. The isocentric mode produces dose distributions comprised of approximately spherical dose clouds around each pseudo-isocenter similar to those in other radiosurgery systems using circular collimators. The non-isocentric mode represents a very different treatment geometry which is more similar to those achieved using multiple pencil beams. From a single node, a modulated fluence pattern can be delivered using multiple beams directed at unique points within the target volume, each of which has an independent field size and beam weight (Figure 3).

The optimal set of relative weighting factors for the candidate beam set (*i.e.,* the dose delivered per beam) is obtained by inverse planning methods that are described later. After optimization the 3D patient model includes the position and orientation of each treatment beam in a stereotactic coordinate system defined by the target anatomy itself or an internal surrogate fixed relative to it (*i.e.,* in target space), together with the field size and monitor unit (MU) setting of each beam. This information is stored as part of a treatment plan and is transferred to the treatment delivery system via the database server.

Treatment Delivery

Beam alignment at the time of treatment is based on automatic registration of digitally reconstructed radiographs (DRRs) generated from the 3D patient model, with live images acquired using the X-ray imaging system in the treatment room. This results in two independent transformations, one for each of the live image and DRR pairs, which are combined and converted into a 3D transformation by geometric backprojection. Since the geometry of the X-ray imaging system relative to the treatment room is known (*i.e.,* in room space) this transformation allows the transformation between room and target space to be obtained. Moreover, since the geometry of the couch and robotic manipulator are known in room space, this transformation allows the pose (*i.e.,* position and orientation) of each treatment beam relative to the target volume that was simulated on the TPS to be achieved during treatment.

At the start of every treatment, the X-ray image guidance system aligns the patient using an adjustable treatment table.
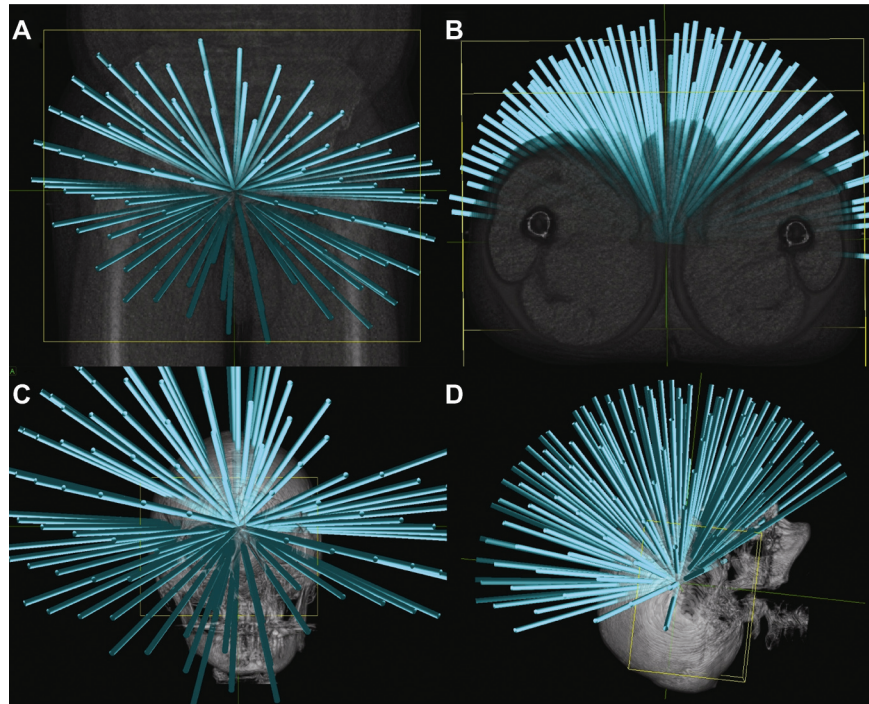
Figure 2: Illustration of the CyberKnife System treatment beam geometry. These beam sets show the isocentric beam generation mode, with a single pseudo-isocenter in each case. The number of nodes contained in the path sets shown here are 96 for the extracranial case (**A-B**) and 125 for the intracranial case (**C-D**). The system is preconfigured with a range of path sets for intracranial and extracranial treatments, including the large general purpose path sets shown here, path sets with anatomy specific nodes (*e.g.,* for treatment of prostate cancer or trigeminal neuralgia), and path sets with smaller numbers of nodes to minimize treatment time by reducing the amount of robot motion. All path sets provide a non-coplanar beam geometry. The appropriate selection is made manually based on the treatment type.

Both a five-axis table and a six-axis RoboCouch® Patient Positioning System, shown in Figure 1b, are available. With the five-axis table the sixth correction (yaw angle) can be applied manually. The purpose of this initial alignment is to reduce the corrections that will be required from the robotic manipulator below maximum limits, which are ±10 mm or ±25 mm in each direction and ±1° to ±5° about each axis depending on the tracking mode, path set, and couch design. After the patient is aligned within these limits, the image guidance system determines the additional translational and rotational corrections needed to precisely align each treatment beam. These corrections are relayed to the robotic manipulator and used to automatically compensate for small target movements by repositioning the LINAC, *i.e.,* fine alignment is achieved uniquely by adjusting the beam position and orientation relative to the patient and not the patient relative to the beam.

During treatment, the robot moves in sequence through the nodes selected during treatment planning. An optimized path traversal algorithm allows the manipulator to travel only between nodes at which one or more treatment beams are to be delivered, or through the minimum number of additional zero-dose nodes required to prevent the robot trajectory intersecting fixed room obstacles or a 'safety zone' surrounding the couch and patient. At each node, the manipulator is used to re-orient the LINAC such that each beam originating at the node can be delivered.

Image acquisition, target localization, and alignment corrections are repeated continually during treatment delivery, typically every 30–60 s; the imaging interval can be adjusted during treatment based on the stability of the target position. The robotic manipulator compensates for small translations and rotations based on the corrections obtained from the most recently acquired image pair; large translations and rotations automatically pause the treatment and prompt the operator to reposition the patient before proceeding. The repositioning can be performed automatically using the RoboCouch table for all translations and rotations, or automatically using the five-axis table for all translations and rotations except the yaw angle. Dose placement accuracy is assured by imaging and correcting beam aim frequently throughout each treatment fraction. No stereotactic frame is required, and one need not assume that motion will not occur after initial patient setup. For targets that move due to respiration an additional tracking system enables beams to move in real time to follow the target while the patient breathes freely.
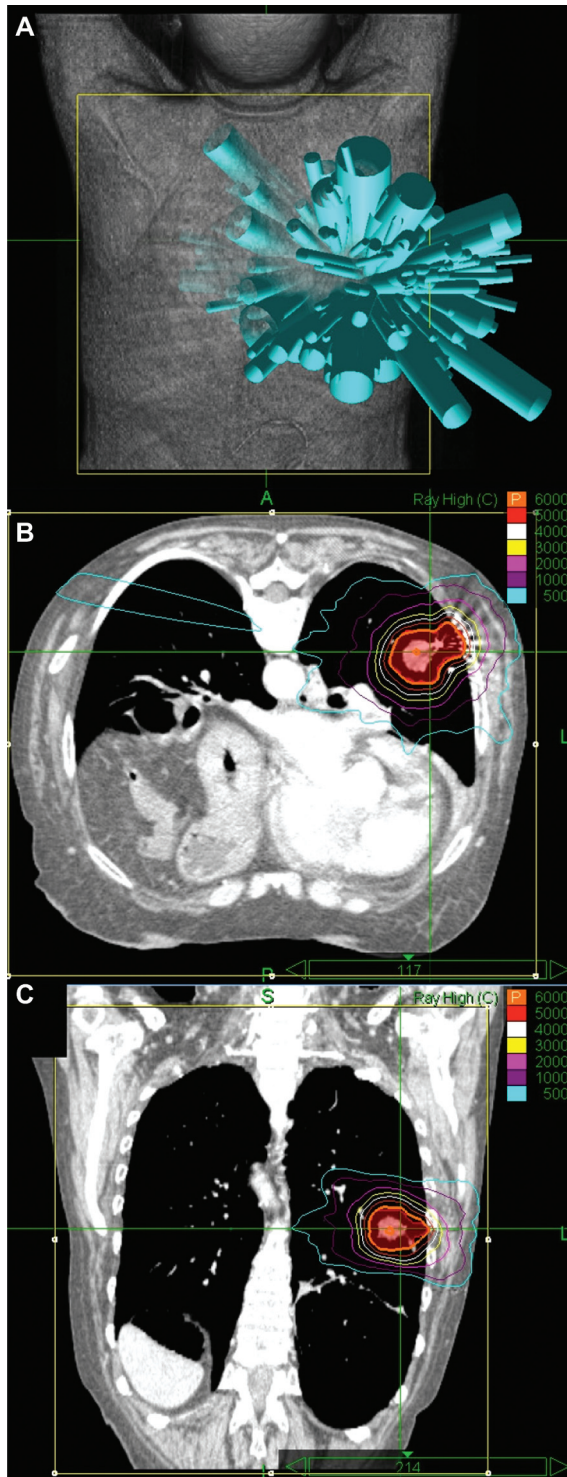
Figure 3: A lung treatment plan generated using a non-isocentric candidate beam set and multiple field sizes. Inspection of the beam geometry (**A**) shows that multiple beams originate at most nodes, and these beams have variable field sizes and beam weights (indicated by the length of the cones). The effect of this fluence-modulated dose distribution delivered from each node is to achieve a highly conformal dose distribution with the irregular target volume, and the combination of beams from a large non-coplanar workspace allows a steep dose gradient in all directions to be achieved

Major Subsystems

Treatment Delivery System Hardware

LINAC: The LINAC uses an X-band cavity magnetron and a standing wave, side-coupled accelerating waveguide, to produce a 6 MV X-ray treatment beam with a dose-rate of 1000 cGy/min. The compact design allows a configuration that does not require a bending magnet. There is also no beam flattening filter. Secondary collimation is provided using twelve fixed circular collimators with diameters ranging from 0.5–6 cm. These collimators can be fitted manually or automatically using the Xchange® Robotic Collimator Changer. Alternatively, the Iris™ Variable Aperture Collimator (Figure 4) allows the same set of twelve field sizes to be achieved with a single variable aperture, and therefore provides the flexibility to apply any field size at any beam position without the need to swap collimators during treatment (43). Dosimetric calibration of such small circular beams is complicated by the effects of steep dose gradients and electronic disequilibrium that are beyond the scope of this review to describe. However, calibration methods designed specifically for small and non-standard fields are the subject of a recently proposed dosimetric formalism (44), the application of which to the CyberKnife System has been shown to result in calibration uncertainties equivalent to those observed in standard large beams (45).

Robotic Manipulator: The LINAC is mounted on a KR240-2 (Series 2000) robotic manipulator (Kuka Roboter GmbH, Augsburg, Germany) that has a manufacturer specification for position repeatability of better than 0.12 mm, and has six degrees of freedom, allowing it to position the LINAC within a large three-dimensional (3D) workspace around the patient with high precision. The robotic manipulator allows each treatment beam to be directed at a unique point in space (*i.e.*, there is no isocenter) and also removes any coplanar constraint on the beam geometry. This geometric flexibility means that the vault in which the system is installed requires a larger primary barrier than is typical for a gantry-mounted LINAC because the beam directions are much less constrained. As an option, the system can be installed in a 'gantry vault' configuration in which the beam directions are restricted to respect the limitations of a conventional vault primary barrier on the side walls, with the option of allowing additional beams incident on the inferior wall if this is adequately shielded. The robotic manipulator compensates for changes in target position and orientation during treatment by adjusting the beam

(**B-C**). In this case the isodoses shown are 60 Gy (prescription), 50 Gy, 40 Gy, 30 Gy, 20 Gy, 10 Gy, and 5 Gy. The conformality index of the prescription isodose is 1.13, and the maximum dose at 2 cm from the edge of the PTV is 23 Gy.
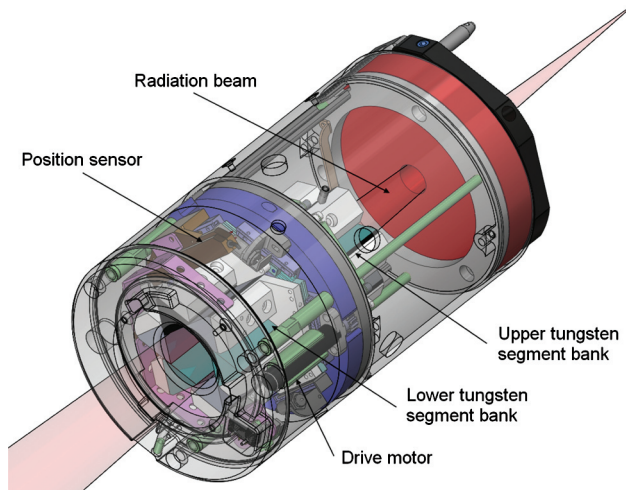
Figure 4: Schematic of the Iris Variable Aperture Collimator highlighting the primary mechanical components. The Iris Collimator contains 12 triangular collimator segments, oriented to define a dodecagon-shaped beam aperture. The 12 segments are divided into 2 banks of 6 segments that are mounted in series, with the 2 banks rotated by 30 degrees relative to each other. This geometry provides an effectively circular beam shape. The design avoids inter-segment leakage without using a tongue-and-groove system because the inter-segment gaps in each bank are covered by the body of a segment in the other bank. Each segment is mounted on a linear bearing; thus, rotational movement of the collimator mounting plate is converted into linear movement of the inner aperture surface for each segment allowing all 12 segments to be driven by a single motor. The aperture can be nearly completely closed (it is limited to 0.025 cm) or opened to a maximum size of 6.8 cm (projected at 80 cm distance). In practice the largest usable opening is constrained by the aperture of the primary collimator. Although the aperture size of the Iris Collimator is essentially continuously variable up to a maximum size 6.8 cm, its use in the CyberKnife System is currently restricted to 12 collimator sizes corresponding to the sizes of the 12 fixed collimators, ranging from 0.5–6 cm, that are available with the CyberKnife System.

position and orientation rather than by moving the patient. This improves alignment accuracy since the manipulator can be moved with greater precision than the patient, who cannot be considered to act as a rigid body attached to the couch. This has guided much of the innovation for the system, *i.e.*, to adjust the beam aim to the target rather than bringing the target in line with the beam.

X-ray Imaging System: Two diagnostic X-ray sources are mounted to the ceiling and illuminate two X-ray detectors by projecting square X-ray fields at 45° from vertical. At the point where the central axes of these beams intersect, the X-ray field size is approximately 15 × 15 cm. The flat panel X-ray detectors, which are mounted flush with the floor, consist of cesium-iodide scintillator deposited directly on amorphous silicon photodiodes and generate high-resolution digital images (1,024 × 1,024 pixels with 16-bit resolution). The X-ray sources and detectors are rigidly fixed, and their projection geometry is calibrated and known in the treatment room coordinate system. Software corrections are applied to

remove the distortion associated with the 45° angle between each detector and the imaging beam central axis (10). The X-ray generators support a range of energies up to 150 kVp.

Stereo Camera System: The positions of optical markers, attached to the patient during treatment, are measured continuously by a stereo camera system mounted on a boom arm attached to the ceiling. There are three CCD cameras within this system. In combination with the X-ray imaging system, this enables the robotic manipulator to track tumors that move with respiration using the Synchrony® Respiratory Tracking System. When not in use, the boom arm can be moved out of the way; exact repositioning of the boom arm is not required.

Treatment Delivery System Software

Image Registration Algorithms

6D Skull Tracking: This method can be used for intracranial targets as well as head and neck targets that are considered to be fixed relative to the skull. Image registration is performed using high contrast bone information contained within the entire field of view. Each 2D registration is performed in multiple stages, using two image similarity measures and several search methods. The resulting 2D transformations for each orthogonal projection are combined and backprojected to determine the 3D rigid transformation that aligns the position and orientation of the skull in the treatment planning CT image with the treatment delivery coordinate system. Fu & Kuduvalli describe this algorithm in detail (46).

Xsight® Spine Tracking: This method can be used for targets located anywhere in the spine, or targets located near the spine and considered to be fixed relative to it. As with the skull tracking method, image registration is based on high contrast bone information. For spine tracking, however, image processing filters are applied to enhance the skeletal structures in both the DRR and the treatment X-ray images. This improves estimation of local displacements for these structures. Optionally, the DRRs can be generated by restricting attenuation to voxels within a region surrounding the spine such that the DRRs represent only spine anatomy and do not include image artifacts from tissue motion or from non-spinal bony anatomy such as the rib cage. Registration is performed in a region of interest (ROI) that generally includes the vertebra of interest plus the two adjacent vertebrae. The local displacement vector that aligns a point in the DRR image with the corresponding point in the X-ray image is estimated at each node point in a grid laid over the ROI. A small region or block surrounding the node point in the DRR image is compared with regions in the X-ray image. Block matching, which

is essentially the estimation of local displacements of skeletal structure, is performed in a multi-resolution approach to increase efficiency and robustness. The position (translation) and orientation (rotation) of the skeletal anatomy, and thus the target, is computed from the resulting local displacement fields between the X-ray image and the DRR image. Details of this algorithm have been described elsewhere (47-49).

Xsight Lung Tracking: This method can be used to track tumors located within the lung without the use of implanted fiducial markers. The lung tracking approach differs from other tracking methods in that patient alignment and tumor tracking are performed in two stages rather than one. Xsight Lung Tracking begins with global patient alignment, including both position and orientation, using the region of the spine nearest the lung tumor. Global alignment happens only once, at the beginning of treatment. After the patient is globally aligned, the treatment couch moves the patient from the spine alignment center to the tumor treatment center (these are defined during treatment planning). After this movement, the tumor will be close to the reference position around which it will move during breathing. Direct tumor tracking is performed by image registration of the tumor region in the DRRs to the corresponding region in the treatment X-ray images. Specifically, the image intensity pattern of the tumor region in the DRR is matched to the most similar region in the X-ray image. A matching window for the tumor is defined based on the tumor silhouette in each projection. The registration process is conducted separately for each projection, resulting in 2D translations for each projection; the 3D tumor translation is determined by backprojection of the 2D translations. This requires that the image intensity pattern of the tumor is distinguishable from other objects in the image, which requires the tumor to have sufficient contrast relative to the surrounding region. The two primary factors that determine tumor visibility are size (which influences contrast) and location (which can influence contrast if the tumor is superimposed in the X-ray image on radiopaque structures such as the spine or mediastinum). The tracking algorithm works best for tumors larger than 15 mm in diameter that are located in the peripheral and apex lung regions. Retrospective analysis of clinical image data for more than 100 patients suggests that the Xsight Lung Tracking system may be appropriate for treating slightly more than 50% of lung radiosurgery candidates (50). The treatment planning system also provides a quality review of the tracking DRRs to help confirm patient eligibility for lung tracking. This tracking method can be combined with the respiratory tracking system described later. The original algorithm is described in detail by Fu *et al*., (51). Recent enhancements include DRRs generated from local tumor neighborhoods, an automatic preferred projection epipolar constraint, tumor template matching allowing for in-plane rotations, and automatic X-ray image enhancement (50).

Fiducial Marker Tracking: This method can be used for soft tissue targets that are not fixed relative to the skull or spine (*e.g.,* prostate, pancreas, liver), including lung tumors for which the Xsight lung tracking method is unsuitable. Radiopaque fiducial markers are implanted in or adjacent to the lesion being treated to provide an internal frame of reference. Cylindrical gold seeds are often used, with dimensions of 0.8–1.2 mm in diameter and 3–6 mm in length. Fiducial markers are often implanted percutaneously under image guidance. Implantation in the lung can also be performed bronchoscopically (52, 53). Between three and five fiducial markers are typically implanted, and in most instances the treatment planning CT scan is acquired a week or more after implantation to allow the fiducial marker positions to stabilize. Fiducial markers are identified in the planning CT scan and therefore their positions are known in the DRR images. Image registration is based on alignment of these known DRR positions with the marker locations extracted from the treatment X-ray images. This process is described in detail elsewhere (54-56). An assessment of potential marker migration is made automatically by determining individual marker misalignment after registration, allowing individual markers to be omitted from the registration calculation if necessary.

Adaptive Image Acquisition Algorithms

The interval between successive image acquisitions and alignment corrections is adapted throughout each treatment fraction based on the intra-fraction stability of the target position and orientation. Generally, the user specifies a maximum interval between image acquisitions at the start of treatment delivery. Before each treatment beam is delivered the time elapsed since the most recent X-ray alignment images were acquired is compared against this limit, and if it is exceeded then a new set of alignment images are acquired and corrections applied before the beam is delivered. The current translational and rotational corrections are displayed numerically on the delivery console, and the history of all corrections observed during the treatment is displayed graphically. Using this information the user is able to adjust the imaging interval during treatment so that the alignment correction frequency is higher when the target position is more variable, and vice versa. In addition, the user is able to manually interrupt the treatment at any time to perform image acquisition.

An extension of this concept for prostate treatment is the InTempo™ Adaptive Imaging System, the intent of which is to automatically increase the frequency of alignment corrections during periods of rapid target motion (Figure 5). Here, the user specifies a 'maximum image age' at the start of treatment delivery. Before each treatment beam is delivered the time elapsed since the most recent X-ray alignment image was acquired *plus* the estimated time required to deliver

the next beam (i.e., the estimated image age) is compared against this limit; if the limit is exceeded then a new set of alignment images are acquired and corrections are applied before the beam is delivered. In addition to the maximum image age, maximum thresholds on inter-image translational and rotational changes are also set. Whenever new images are acquired the change in target position from the previous set of images is compared against these thresholds. If the position change is lower than the thresholds then treatment continues as normal, but if either threshold is exceeded (thereby indicating a high degree of motion of the target) then either the

maximum image age is automatically set to its minimum limit of 15 s, or treatment is paused, at the user's discretion.

Synchrony Respiratory Motion Tracking System

The Synchrony Respiratory Tracking System provides real-time tracking for tumors that move with respiration. Alignment of each treatment beam with the moving target is maintained by moving the beam dynamically during treatment, achieving a 100% duty cycle while the patient breathes normally throughout treatment without the need for breath-holding.

Figure 5: The treatment delivery graphical user interface (GUI) during a prostate treatment using fiducial marker tracking and the InTempo adaptive imaging algorithm. The section labeled 'couch corrections' (to the right of the X-ray images) shows the target's actual position relative to its ideal aligned position. These offsets are compensated for by realigning the beam with the target using the robotic manipulator. At the base of the screen, the history of translational (left side) and rotational (right side) corrections applied during this treatment fraction are shown. The position corrections are inferior-superior (blue), anterior-posterior (green), left-right (red), and total 3D offset (black). The rotation corrections are pitch (red), roll (blue), and yaw (green), with the sum of all angular offsets shown in black. During this treatment the first seven images are acquired with a maximum image age of 30 s. Between images 6 and 7 the prostate moves by about 3 mm, which automatically triggers the maximum image age to be reduced to 15 s, resulting in more frequent position corrections being applied (note reduced interval between images 7-12). Importantly in this case, a baseline shift in the pitch angle of 2-3° is observed during the first four minutes of treatment that would have been missed if intra-fraction corrections were not applied. With correction, this rotation is reduced to a more randomly distributed inter-correction error of about 1° on average.

The primary system concept is a correlation between tumor position and external marker position. To minimize radiographic imaging exposure, episodic imaging is combined with continuous measurement of an external breathing signal (57). At the start of treatment, the tumor position is determined at multiple discrete time points by acquiring orthogonal X-ray images and using either the fiducial marker or Xsight Lung tracking methods described above. A linear, quadratic, or constrained fourth order polynomial correlation model is generated by fitting the tumor positions at different phases of the breathing cycle to the simultaneous external marker positions. To ensure that the full motion range within the breathing cycle is evenly sampled, the X-ray imaging system can be automatically triggered based on the external breathing signal. An important feature of this method is its ability to fit different models to the inhalation and exhalation phases. During treatment, the internal tumor position is estimated from the external marker positions using the correlation model, and this information is used to move the linear accelerator dynamically with the target.

Three optical markers attached to a vest worn by the patient are used to provide the external signal. Light-emitting diodes (LEDs) transmit light through optical fibers that terminate at each marker. This approach was chosen over directly attaching LEDs to the vest to avoid the presence of copper wire in the X-ray images. The optical markers are sequentially strobed and a stereo camera system measures their 3D positions continuously at a frequency of approximately 30 Hz.

A schematic block diagram of this system is shown in Figure 6. There is a separate correlation model for each external marker (each of which is in fact composed of three independent models, describing the correlation of external marker position with internal target superior-inferior, anterior-posterior, and left-right position, respectively). Each model provides an estimate of the target position, and these individual estimates are averaged to get the final position estimate. Ideally, this value
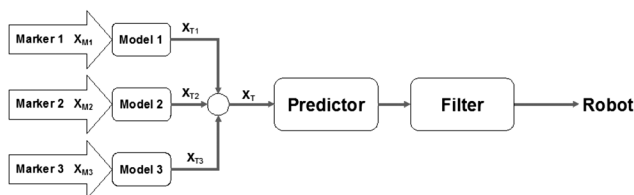

Figure 6: Schematic block diagram of the Synchrony Respiratory Tracking System. For each external marker, there is a correlation model between the position of the internal target and the position of the external marker. The outputs of the individual models are averaged to obtain the present time estimate of the target position. A predictor is used to compensate for communication latencies and robotic manipulator inertia. Finally, the predicted position is filtered and sent to the robotic manipulator as a position command. Reproduced with permission from Sayeh *et al.,* (58).

can be sent directly to the robotic manipulator. However, communication latencies along with robotic manipulator and LINAC inertia cause delays, which total 115 ms in the current system; if the present time target position estimate is sent to the robot, there will be a lag in the robotic manipulator's motion. A predictor is used to compensate for these delays using the history of the target movement. The current predictor uses a hybrid model that generates multiple predictions at each instant, together with a heuristic method for selecting between them. The predictor is adaptive and is designed to respond quickly to changes in the breathing pattern and target movement. The output of the predictor is passed through a smoothing filter before it is sent to the robot as a position command. Further details are described in Sayeh *et al.,* (58).

Inter- and intra-fraction respiratory motion changes are common and well reported (59-61). By generating the correlation model at the beginning of every treatment, inter-fraction variability is accounted for. However, since the target motion typically changes during treatment it is important to check and update the model during treatment. This is accomplished by acquiring additional X-ray images periodically during treatment. The target position predicted by the model is compared with the actual position determined from the images. The correlation model error, which is the distance between the predicted and actual positions, is computed and displayed graphically. If the error is larger than a predefined value, the treatment is automatically paused; the model can then be checked with additional X-ray image acquisitions or completely regenerated. If the model accuracy is adequate, the newly acquired data point is used to update the model. Thus, the correlation model adapts to gradual changes in target position and motion during treatment. The maximum number of model data points is 15. If there are already 15 data points, the new data point is added and the oldest data point is deleted.

Treatment Planning System Software

Multimodality Image Registration and Volume Definition Algorithms

A volumetric CT scan is required by the X-ray image-guided tracking system, and for the 3D patient model needed to simulate the non-coplanar treatment beam geometry. Up to three additional 3D image sets can be loaded simultaneously and registered to this CT scan, *e.g.,* MR, PET, 3D rotational angiography, or additional CT images. Image registration and fusion can be performed by maximization of mutual information (62, 63), by aligning manually identified anatomic landmarks or semi-automatically determined fiducial marker positions, or by manual alignment. Target volumes, organs at risk, and other structures can be defined on any of these images in any of the cardinal image planes. In addition, male

pelvic anatomy (prostate, bladder, rectum, seminal vesicles, and femoral heads) can be contoured using a shape model-based segmentation algorithm with minimal user interaction.

Dose Calculation Algorithms

A ray-tracing algorithm provides a fast dose calculation method based on measured beam data look-up. Heterogeneity correction is performed using effective path length, and obliquity correction is performed by casting multiple rays within each beam. Alternatively, a Monte Carlo dose calculation algorithm uses a measurement-based virtual source representation of the LINAC head to simulate each treatment beam. The algorithm, which is implemented in parallel, performs treatment plan dose calculations in generally less than five minutes for a calculation uncertainty of 2% on the standard TPS hardware, which has 8 processors. The dose and random uncertainty at each voxel is calculated, and the raw dose distribution can be smoothed using a range of filters. This algorithm has been described by Ma *et al.,* (64) and has been compared against measurements in heterogeneous phantoms (65-67). The Monte Carlo dose calculation can be used as the basis of plan optimization, therefore this algorithm minimizes both the dose calculation and optimization convergence errors in situations where the ray tracing algorithm can not provide sufficient accuracy, *e.g.,* in lung tumor treatments. Dose calculation for lung radiosurgery using relatively simple algorithms such as ray tracing or pencil beam convolution provide only an estimate of the effect of the increased electron range in low density lung tissue on PTV and OAR doses. Now that more accurate dose calculation is possible with Monte Carlo algorithms, differences between the doses actually delivered and previously estimated, and the clinical and research consequences of these differences, are being evaluated (68, 69).

Beam Weight Optimization Algorithms

This is performed in a two-step process. First, candidate beams are generated and their dose distribution is calculated. Second, the relative weight of each beam is optimized by minimizing a cost function defined by the similarity of the resulting dose distribution to dosimetric and MU goals specified by the user. This approach can be considered as a form of direct aperture optimization, since there is no simplified bixel representation of the candidate beams during optimization. Currently three algorithms are available for the second part of this procedure, which are described below in historical order.

Simplex Optimization: The original optimization method formulated the cost function, *F*, as a weighted sum of the deviations from user specified maximum and minimum dose

objectives for each structure (or other manually defined points), plus the total MU setting,

$$F = \sum x_j + \sum \Omega_i \delta_i \qquad [1]$$

where x_j is the MU setting of beam *j*, δ_i is the deviation from the ith user specified maximum or minimum dose goal and Ω_i is the weighting factor associated with this objective. This function is minimized by optimizing the MU settings of all candidate beams using the Simplex method, which finds the global minimum cost function value. Optionally, any of these minimum and maximum dose goals can be defined as fixed constraints such that the solution must satisfy them. Similarly, fixed constraints can be defined for maximum MU per beam and per node, and for minimum MU per beam. A limitation of this method is the possibility to define an infeasible problem, in which the combination of minimum and maximum fixed constraints prevents a solution from being possible. For example, there might be no solution that meets both the maximum dose fixed constraint on an OAR and the minimum dose fixed constraint on the PTV if these structures are adjacent and the difference between the constraints is too large. In addition, there is no progress update during optimization, so the user is unable to assess whether the solution is developing as desired, or whether to interrupt and modify the problem. A further limitation, in common with all approaches in which the multiple conflicting optimization goals are combined in a single cost function and then optimized simultaneously, is that the solution is highly dependent on the manually selected weighting factors, and these cannot generally be set intuitively. In practice these two limitations mean that this method is usually performed in multiple iterations until a feasible problem is specified that results in a clinically acceptable dose distribution.

Iterative Optimization: The problem of infeasibility was overcome with the introduction of the Iterative Optimization algorithm, by removing fixed constraints. In this approach the cost function is formulated as a weighted sum of maximum and minimum dose deviations from user defined goals. The optimum set of beam weights is achieved through an iterative search strategy similar to gradient descent. Initially, each candidate beam is assigned an MU setting based on the ratio of the total dose it delivers to all points within the target volume relative to all points within the patient (the larger this ratio, the larger the initial MU setting). The iterative algorithm then considers the effect of increasing and decreasing the MU setting by a fixed increment of each beam in turn, and retains the setting that gives the largest reduction in cost function. When no further reduction is possible by altering any beam weight, the increment is reduced and the process repeats. The algorithm also incorporates beam retargeting, where a proportion of the candidate beams with zero MU are

retargeted at areas of low dose within the target volume to form new candidate beams. In addition to avoiding infeasible problems, this approach has the advantage of providing feedback in the form of an isodose display and dose-volume histogram (DVH) updates at the end of each iteration. In common with the Simplex algorithm though, the reliance on simultaneous optimization of multiple conflicting dose objectives requires the use of non-intuitive manual weighting factors. In addition, the lack of maximum MU constraints, or a total MU term within the cost function, tends to deliver solutions with a significantly larger number of beams and total MU than achieved with the Simplex algorithm, and the absence of maximum fixed dose constraints means that achieving acceptable maximum doses to OARs is more difficult.

Sequential Optimization: This method retains the main advantages of the Simplex method: i) global minimum value for the cost function is achieved, ii) limitation and optimization of total MU, iii) maximum dose fixed constraints can be used; and the advantages of the Iterative method: i) interactive feedback during optimization, and ii) avoiding infeasible optimization problems. At the same time, this method avoids the need for manual weighting factors to signify the importance of conflicting goals in the cost function. The method is an example of stepwise multi-criteria optimization, and the underlying approach is described in detail elsewhere (70). The process starts with user defined fixed constraints on maximum dose for each target volume and OAR, and for maximum MU per beam, per node, and total

MU. The optimization problem is formulated as a series of steps. At each step a cost function corresponding to just one clinical objective is defined, and this is minimized subject to existing dose and MU constraints using the Simplex method. The possible objectives are to optimize minimum dose, optimize dose coverage (maximize the integral dose below a user defined goal), optimize homogeneity (maximize the integral dose below the maximum dose fixed constraint), optimize conformality (minimize the maximum dose to a shell structure surrounding the target), optimize maximum dose, optimize mean dose (minimize the integral dose above a user defined goal), and optimize total MU setting. Each objective can only be applied to a single structure in any optimization step, except for total MU which is not linked to any structure. The result of each step is applied, with optional relaxation, as an additional constraint to be respected by all subsequent steps. Therefore, the optimization process involves contractive constraint mapping, with the available solution space reducing at each step. In contrast to the simultaneous optimization of multiple objectives used in both previous algorithms, this approach has several advantages:

- Numerical weighting factors are not needed. Instead, clinical judgment is used more directly to place the optimization steps in order of clinical priority
- The result of each step cannot be degraded during any later step beyond the optional relaxation applied to it. Therefore the solution progresses predictably
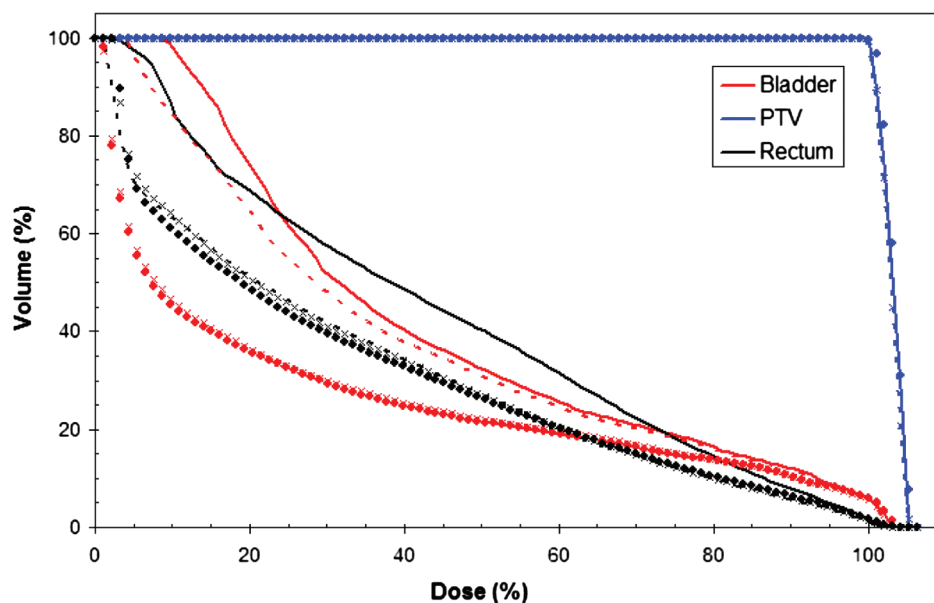

Figure 7: A dose volume histogram showing the results of a four-step Sequential Optimization script for the prostate. Step 1 (solid lines) maximizes the PTV coverage by the 100% prescription isodose. Step 2 (dashed lines) minimizes the mean rectal dose. Step 3 (crosses) minimizes the mean bladder dose. Step 4 (circles) reduces the number of beams from 303 to 173. This example illustrates the predictable nature of the plan improvement at each step because the optimization objective achieved at each step is not degraded by any subsequent step.

- The solution at each step is guaranteed to be feasible, because constraints are based on results achieved in previous steps (*i.e.,* it is impossible to specify an optimization problem which has no solution)
- This method enables efficient evaluation of the trade-offs between clinical objectives because the result at each step is limited only by the constraints obtained in previous steps, and the binding constraints are easily identified.

Taken together, these advantages allow for a more systematic approach to treatment planning than is possible through the iterative variation of multiple weighting factors (70).

Once an appropriate sequence of optimization steps is identified, they can be stored as a script and applied to similar, future clinical cases. Such scripts can substantially reduce planning time for both typical and challenging cases and potentially allow higher quality treatment plans to be generated consistently (71). An example of an optimization script, including use of the beam reduction tool described in the next section, is shown in Figure 7.

Treatment Efficiency Optimization Algorithms

In the Sequential Optimization algorithm, three post-processing tools are provided that enable the user to evaluate trade-offs between treatment efficiency and dosimetric quality in order to obtain a clinically optimal treatment plan. The 'Beam Reduction' tool removes all beams with an MU setting lower than a user-defined threshold from the set of candidate beams in the current solution, and then at the user's discretion either repeats the sequential optimization script with this reduced beam-set or simply rescales the MU

settings of the remaining beams such that the original prescription dose is delivered. Since at this point the great majority of candidate beams have zero MU, and all of these are removed in the beam reduction step, the subsequent re-optimization is much faster than the initial optimization. The 'Node Reduction' tool orders nodes in terms of the total MU, or the total of MU multiplied by the beam area, of all beams at each node in the current solution (the latter method is designed to bias the algorithm to retain nodes where larger beam sizes are used). Nodes are removed in order from the bottom of this list until the number of nodes in the candidate beam set is equal to a user-defined value, and then the sequential optimization script is repeated with this reduced candidate beam-set.

Finally, the 'Time Reduction' tool employs a combination of these approaches to reduce the treatment time to an explicit user-defined goal. An iterative procedure removes beams and nodes at each step according to hard-coded heuristics and the sequential optimization script is repeated. After each step, the treatment time is estimated, including time for beam-on, robot motion, image acquisition and processing, and a non-specific 'set-up' time defined by the user. If the estimated treatment time is greater than the goal time then a further iteration is performed. This algorithm automatically adds new candidate beams after the beam and node reduction in order to increase the solution space available with each reduced node-set. Iterations continue until either the treatment time goal or a minimum number of nodes, or beams, is achieved. The result of each iteration is stored as part of a solution history, which enables the trade-offs between treatment time and dosimetric plan quality to be quickly evaluated at any iteration, and the clinically optimal treatment plan to be selected.
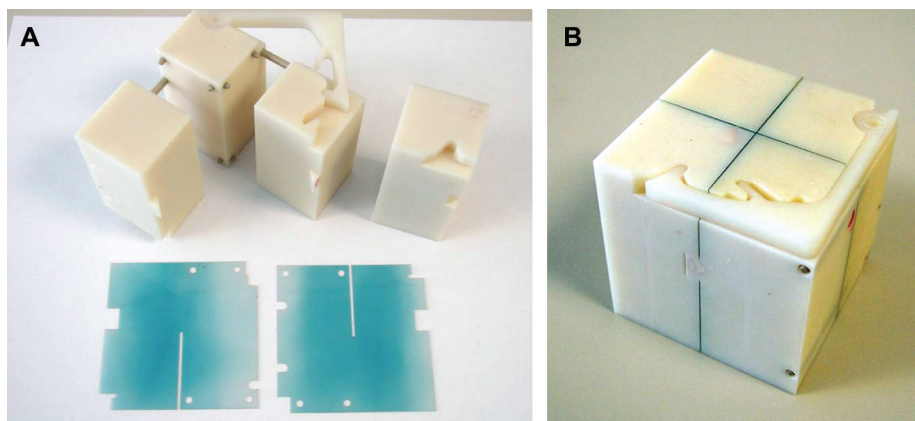

Figure 8: The ball cube test object and radiochromic films that are used for TSE measurements with the CyberKnife System. (**A**) The test object components, including the films with laser cut notches to facilitate their assembly within the ball cube. (**B**) The test object assembled, with the films sandwiched between the four block segments. The purpose of the laser cutting and the complex clip arrangement used to assemble the device is to obtain a measurement precision that is better than the sub-millimeter tolerance applied to the results of this test. In addition to the test object, anthropomorphic phantoms into which the object is placed to enable testing of the full range of tracking modes, and software to analyze the scanned films, are available from the vendor.

Table II

Phantom TSE measurements (mean ± SD) with static phantoms. N is the number of CyberKnife Systems on which measurements were performed, and M is the total number of measurements in each study.

Targeting Mode	TSE (mm)	N	M	Ref
3D Skull tracking (2003)	1.1 ± 0.3	1	23	(73)
6D Skull tracking (2003)	0.4 ± 0.2	2	8	(74)
6D Skull tracking (2008)	0.4 ± 0.1	1	5	(10)
Fiducial tracking (2003)	0.4 ± 0.2	2	6	(74)
Fiducial tracking (2004)	0.7 ± 0.3	3	16	(101)
Fiducial tracking (2008)	0.3 ± 0.1	1	5	(10)
Xsight Spine tracking (2007)	0.5 ± 0.2	1	10	(86)
Xsight Spine tracking (2008)	0.6 ± 0.3	1	7	(49)
Xsight Spine tracking (2008)	0.5 ± 0.2	1	5	(10)
Xsight Lung tracking (2007)	0.9	1	1	(51)

Geometric Accuracy

Phantom-based Accuracy Measurements without Respiratory Motion

While the accuracy of each component in the treatment process that contributes to geometric accuracy can be tested independently, it is most meaningful to assess the *total system error* (TSE) of treatment planning and delivery, an error measure that was first developed for testing the accuracy of frame-based stereotactic surgery and was originally termed total clinically relevant error (72). The TSE can be measured using a hidden test object containing two radiochromic films positioned orthogonally within a spherical target structure that is placed within an anthropomorphic phantom (Figure 8). The phantom is subjected to the entire treatment process (CT scan, target volume delineation, plan generation, treatment delivery) including all data transfer steps. A treatment plan is designed to conformally treat the target structure, and the phantom is aligned and treated in the same manner as a patient. The TSE is the radial offset between the center of the dose distribution measured from the film and its intended position (the geometric center of the target). Therefore, the measurement includes sources of uncertainty present in the entire treatment process, from image acquisition to treatment delivery.

Published results of these tests for the skull tracking, fiducial tracking, Xsight Spine, and Xsight Lung tracking methods are summarized in Table II. It should be noted that the skull tracking results presented by Chang *et al.*, (73) were obtained with the earliest version of the skull tracking algorithm that did not correct for the effect of skull rotation on beam alignment (see Table I). Data obtained from this same unit after upgrade to the current 6D tracking algorithm is included in the study by Main *et al.,* (74), and shows a significant improvement. A dependence on CT slice interval was observed, with mean TSE worsening by 0.7 mm when the slice interval increased from 1.25 mm to 3.75 mm (73), presumably owing to an increase in the superior-inferior localization uncertainty. For fiducial tracking, theoretical studies also demonstrate an improvement in tracking accuracy with increasing numbers of fiducial markers, although this becomes insignificant when the number exceeds five (75).

Clinical Data-based Accuracy Measurements without Respiratory Motion

The above tests were performed using static phantoms, and therefore the results do not include the impact of residual intra-fraction patient movement between successive X-ray image acquisitions on targeting accuracy. Hoogeman *et al.,* (76) analyzed tracking information stored in treatment log files to study the intra-fraction target motion of 57 patients treated for intracranial, head and neck, and spinal indications. All treatments involved non-invasive immobilization including carefully fitted thermoplastic masks and head rests (for intracranial, head and neck, and upper spine targets), and vacuum formed bags (for spine targets). Spine patients were treated in either a supine or prone position. Alignment X-ray

Table III

Effect of intra-fraction motion on translational and rotational alignment offsets for intracranial and spine treatments with the patient in a supine position. Rotational offsets were calculated separately about the superior-inferior, left-right, and anterior-posterior axes and the ranges are shown. The data for 30 minute elapsed time are calculated by linear extrapolation of Hoogeman *et al.,* data, based on the trend observed in that study (89). The Murphy study (77) analyzed the spine data by anatomical level, and the ranges are shown. Note also that the effect of couch movements on calculated offset was considered in (89) but ignored in (77), which means that the offsets presented for elapsed times of 15-45 minutes in (77) are underestimated to some degree.

Elapsed Time (minutes)	Systematic Intra-fraction offset from initial position (2 SD)				Ref
	3D Translational Offset (mm)		Rotational Offset about each axis (°)		
	Intracranial	Spine (Supine)	Intracranial	Spine (Supine)	
1-2	< 0.2	< 0.4	< 0.15	< 0.15	(89)
15	1.6	2.4	0.6-1.0	0.6-1.0	(89)
30	3.2	4.8	1.2-2.0	1.2-2.0	
1-2	0.4	0.4-0.6	-	-	(77)
15-45	2.6	2.0-2.6	-	-	(77)

images were acquired every 1-2 minutes during treatment, and the translation and rotation offsets were obtained from treatment logfiles. By comparing the offsets at each instant against those calculated at some previous time, intra-fraction motion was evaluated as a function of the elapsed time between image acquisitions.

Using this approach the uncorrected intra-fraction motion (*i.e.,* assuming that alignment corrections were not performed using the CyberKnife System) was calculated over varying periods of up to 15 minutes. The maximum translational offset observed in any direction over a 15-minute period was 3.8, 4.3, and 12.3 mm for the intracranial, supine spine, and prone spine cases, respectively. Respiratory motion was noted as the cause of the larger offsets for the prone patients. Considering only the supine data, the systematic 3D translational and rotational offsets, quantified as two standard deviations (SD) above the population mean, are shown in Table III. These data demonstrate that the difference between initial target position and mean target position during the subsequent 15-minute period is frequently more than 1 mm, and may be as high as 1.6 mm to 2.4 mm for any individual patient in this population. Table III also shows the estimated systematic offsets that would be expected with a 30-minute period are double these values, based on an observed trend for these offsets to increase linearly with time (76).

It can be seen that ignoring intra-fraction motion will lead to systematic translational errors in beam alignment of 1-5 mm for a substantial proportion of patients, assuming that the target volume is at the center of the skull or spine and the time between alignment image acquisition and the end of treatment delivery is 15-30 minutes. If the target is displaced from the center then additional alignment errors occur because of the systematic rotational offsets of up to 0.6°–2.0° about each major axis. By comparison, the systematic translational offset observed over the CyberKnife inter-image period of 1–2 min (after each of which beam aim was corrected by the system) was <0.2 and <0.4 mm (2 SD) for intracranial and supine spine cases, respectively, and the systematic rotational offset was <0.15 degrees (2 SD) in each rotation direction

for both groups. Recently, Murphy has analyzed the residual intra-fraction motion observed in a larger group of 577 CyberKnife treatment records corresponding to 273 patients treated for intracranial and spinal targets (77). Although these patients were all treated in 1999-2002 using older versions of the tracking algorithms, and the method of analysis is different than that described by Hoogeman et al, the resulting systematic translational offsets observed over an imaging period of 1-2 minutes was only slightly greater, being 0.4–0.6 mm (Table III). These studies demonstrate that the systematic residual alignment error over the interval between alignment corrections for intracranial and spine patients during CyberKnife treatment is small, which is not the case when intra-fraction motion is ignored.

Random offsets during treatment due to intra-fraction motion, which have a much smaller dosimetric impact than systematic errors (78), were analyzed as the population mean of the standard deviations observed within each treatment fraction about the mean position during that treatment. This was found to be less dependent on the interval between image acquisitions than the systematic offsets (76). The mean 3D random translational offsets quantified in this manner were approximately 0.3 mm and 0.7 mm for intracranial and supine spine, respectively, over an imaging period of 1-2 minutes in the Hoogeman *et al.*, study (76), but larger values of 1.0 mm and 1.2-1.3 mm were found for the same treatment sites in the study using older data (77). The most recent analysis of random alignment error during spine treatment with the CyberKnife System due to target motion between images was performed by logfile analysis of 260 patients, with an average imaging interval of 1.5 minutes (79). This showed the mean inter-image 3D shift in target position to be 0.5 mm, but this was not reduced into systematic and random components in the analysis. Moreover, this study found the dosimetric implications of these offsets in the worst case to be a decrease in target volume covered by the prescription dose of 1.7%, and an increase in the spinal cord covered by the 8 Gy tolerance dose of 0.05 cm^3. One small study of 6 patients has shown larger offsets, and larger dosimetric consequences due to these offsets (80). The reason for differences between this

Table IV

Phantom TSE measurements with Synchrony respiratory motion tracking. Accuracy results are presented as *Relative radial error in addition to static targeting error, or **TSE (*i.e.* total radial targeting error). N and M are as defined in Table II.

Waveform	Respiratory Motion Pattern						
	Amplitude (mm) (largest component)	Period (s)	Phase difference (°)	TSE (mm) or relative offset (mm)	N	M	Ref
Sin⁴	25	3.6	0 - 30	0.7 ± 0.3 *	3	9	(84)
Sin⁴	25	3.6	0 - 30	≤ 0.6 **	1	2	(87)
Sin³	25	~ 4	0 - 20	≤ 0.4 *	3	9	(85)
Sin³	25	~ 4	30	≤ 0.8 *	3	3	(85)
Sin³	25	~ 4	0 - 30	≤ 0.6 **	1	5	(102)

study and the studies described above are not clear, but are discussed by Fürweger *et al.*, (79).

Of the treatment sites that do not move significantly due to respiration, the prostate is perhaps that with the greatest potential for large intra-fraction motion (81). Xie *et al.*, performed a logfile-based study, similar to those described above, of intra-fraction prostate motion observed in 21 patients and 105 treatment fractions with the CyberKnife System (82). They concluded that with an imaging interval of 30 s, the target translation between images would be <1 mm in 90% of instances, and if the interval was increased to 60 s this proportion decreased to 81%. The data suggests that since motion patterns are highly variable between patients, and over time for the same patient, longer imaging intervals would be acceptable at some periods during treatment and shorter intervals would be of benefit during other periods, but these patterns are hard to predict. The InTempo prostate tracking method described previously is an attempt to provide such functionality by automatically adjusting the interval between alignment corrections based on the recent history of inter-fraction motion, with a minimum interval of just 15 s. An analysis of the efficacy of this method has not yet been performed, but the logfile method used in all of these studies could be easily applied.

Phantom-based Accuracy Measurements with Respiratory Motion

For targets that move due to respiration the TSE test method has been adapted for the Synchrony System by placing the test phantom on a motion table which moves continuously during treatment to simulate respiratory motion. For these experiments, clinically realistic motion waveforms have been based on the motion of real lung tumors with implanted fiducial markers observed using fluoroscopic imaging from multiple directions (61, 83). The first multi-center study of this type (84) reported the additional radial offset observed relative to the static TSE result (Table IV). This study was conducted using the first release of the Synchrony System which has subsequently been improved (*e.g.,* by the use of non-linear models to better characterize tumor-marker motions exhibiting non-zero phase differences, increasing the maximum number of correlation model data-points from 10 to 15, and improving the prediction algorithm). Data obtained with more recent versions of the Synchrony System are also included in Table IV (85-87).

In addition to shifting the dose centroid, respiratory motion may blur the dose distribution (*i.e.,* reduce the steepness of the dose gradient around the target). This effect was studied using the technique described above. The distance between the 20% and 80% isodose lines was measured in the superior-inferior direction (the axis of greatest motion) at the edges of the target (86, 87). Motion-induced blurring was quantified by the change in the 20-80% isodose distance for treatments with and without motion. The results demonstrate no additional blurring with linear motion, while extreme nonlinear correlation (30 degree phase difference between object and external marker motions) resulted in ≤ 1 mm blurring. This compares to blurring of more than 8 mm when no respiratory tracking was used. A similar experiment has been conducted using a treatment plan with far greater isodose line complexity than typically encountered clinically. Treatment was delivered using simulated respiratory motion with and without Synchrony respiratory tracking; the amplitude of motion was 20 mm, the motion pattern was a $\sin^2(\omega t)$ waveform, and
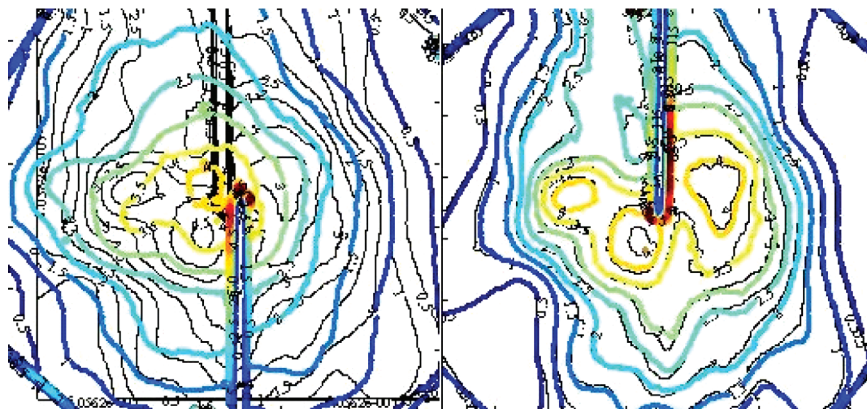
Figure 9: Dose distributions for simulated respiratory motion with (right) and without (left) the use of Synchrony tracking. The underlying black curves are isodose lines generated by the treatment planning system. The colored curves are the same isodose lines measured after treatment delivery with respiratory motion. The isodose lines are displayed in 0.5 Gy increments, with the highest isodose line being 4.0 Gy. The scale is defined by the length of a side of the square dosimetry film, which is 6.3 cm. The amplitude of motion was 20 mm, the motion pattern was a $\sin^2(\omega t)$ waveform, and the period was 7 s. These results show isodose line distance to agreement to be generally better than 1 mm, with a maximum displacement of 2 mm. Images courtesy of Drs. J. P. A. Marijnissen and Y. Seppenwoolde, Erasmus Medical Center—Daniel den Hoed Center, Rotterdam, The Netherlands. Reproduced with permission from Sayeh *et al.,* (58).

the period was 7 s. The results show isodose line agreement to be generally better than 1 mm, with a maximum displacement of 2 mm (Figure 9).

Clinical Data-based Accuracy Measurements with Respiratory Motion

Additional accuracy tests have been performed by retrospective analysis of clinical data. As mentioned previously the correlation model is checked and updated regularly by acquiring additional X-ray images. The correlation model error, which is the distance between the model-based predicted and image-based actual positions, is stored in a log file. This error is a measure of the accuracy of Synchrony tracking in an actual clinical application. In one report, the log files from 14 patients treated at three CyberKnife centers were collected and analyzed (88). The average of 510 correlation error values contained in these log files was 1.4 ± 1.0 mm (mean ± SD). A linear correlation model was used for all cases. More recently, Hoogeman *et al.,* (89) has performed a more comprehensive analysis of the error log files corresponding to 158 lung treatment fractions (49 tumors in 44 patients), in which both linear and quadratic correlation models were used. The mean correlation and prediction model errors in each cardinal direction were assessed during treatment delivery for each fraction. The overall population mean of these mean values was found to be very close to zero (0.0-0.2 mm combined error due to both models), and perhaps more importantly the variation in this mean offset across all treatment fractions was also very low; 0.6 mm (2 SD) in each direction in the correlation model error and 0.0 mm (2 SD) in the prediction model error, which indicates that the systematic tracking error due to modeling uncertainties is small in every patient in this series. The Hoogeman study results place an upper limit on the correlation and prediction model errors that would be expected with the current system version in 2010. The Synchrony version used in that study did not include features standard in the current version such as automatic image acquisition which triggers the X-ray imaging system using the external marker signal in order to more uniformly sample the breathing cycle, the addition of a constrained 4th order polynomial to the set of available correlation models, or the newest hybrid predictor which uses improved prediction models and selection heuristics compared with the hybrid predictor used in the study (this early version is described in (90)). Initial investigations of the current hybrid predictor using a subset of the patient data from the Hoogeman study shows that the instantaneous prediction errors are reduced by 20-30% in comparison with the hybrid results presented in the study.

Seppenwoolde *et al.,* (60) examined the correlation model error for eight lung cancer patients treated with respiratory gating (91). All of these patients had simultaneous and continuous recordings of internal tumor and external marker positions. This data was used to simulate a CyberKnife treatment with Synchrony tracking. The continuous internal tumor position data was used to compute the continuous correlation model error. The use of the linear correlation model achieved low correlation model error in all cases. In the cases with hysteresis, the quadratic model provided some additional improvement in tracking accuracy. The authors concluded that the "combined use of internal and external markers allow the robot to accurately follow tumor motion even in the case of irregularities in breathing patterns". The chest wall and internal target motion for two of these patients was replicated using a sophisticated respiratory motion phantom (92). One patient exhibited a significant phase difference between chest wall and tumor motion, and both exhibited irregular motion amplitude, period, and baseline. For each patient, a treatment plan was delivered twice, once to a static phantom, and once to the phantom during patient specific motion with Synchrony respiratory tracking. The dose distributions measured using radiochromic film for the static and moving treatment cases were compared using a Gamma analysis with a pass criterion of 3% dose difference and 3 mm distance to agreement, which was based on the uncertainty in film calibration and alignment. The proportion of pixels meeting this criterion was ≥ 97% for both patients.

Finally, Wong *et al.,* (93) employed an independent optical tracking system to study the accuracy of individual beam alignment to an artificial moving target. The target and external marker motions were based on motions recorded during three patient treatments. Their equipment allowed the tracking error to be measured as the difference in distance and orientation of the secondary collimator to the target from the average value at all times during treatment delivery. The overall tracking precision, defined as the mean over all beams of the standard deviation of distance and angle observed for each individual beam, was ≤0.6 mm and <0.08 degrees for the three sets of patient motion data.

Clinical Overview

The developments of the CyberKnife System described in this review have resulted in substantial improvements in dose calculation accuracy, treatment plan optimality, treatment delivery geometric accuracy, treatment time, and the range of body sites that are technically accessible to treatment. Most recently, technical developments included in the CyberKnife VSI System have for the first time made practical the delivery of more extended fractionation schemes (such as those common to IMRT).

Clinical development over the years (most of it generated by CyberKnife users themselves) has both prompted technical innovation and has been enabled by it. Early intracranial outcomes (94) prompted improvements in skull tracking (6) that

supported development of a wide range of intracranial applications that are helping to validate the newest skull-tracking algorithm (46). The desire to treat spinal lesions (95) lead to the development of fiducial tracking algorithms (75), which both set the stage for further spinal treatments (*e.g.,* Gerszten *et al.,* (23)) and continued growth of extracranial applications outside the central nervous system (96-98), as well as providing inspiration for the development of the fiducial-free Xsight Spine Tracking system (49). As treatments extended to tumors in organs that move with respiration (97, 98), Synchrony tracking was introduced and tested in phantom studies (60, 93) and in clinical practice (89). Today researchers worldwide are employing the technologies described in this review in daily clinical practice to treat brain (13-17), spine (18-22), lung (24-27), prostate (29-32), liver (33-35), pancreas (99, 100), head & neck (36-40), and emerging applications such as breast (41) and other extracranial sites (42). The total number of patients treated has increased from just 30 in 1999 to over 90,000 in 2010.

Summary

Notwithstanding the technological developments described in this review, it is important to note that the underlying design principles of the CyberKnife System have not changed. Specifically, the CyberKnife System allows the key aspects of radiosurgery to be applied to targets throughout the body. Those key aspects are:

(a) Minimization of the CTV-to-PTV margin. This is made possible by high accuracy of treatment beam alignment and delivery, achieved through the combination of an X-ray image guidance system, which enables frameless stereotactic targeting for all body sites; a robotic manipulator, which enables each beam to be aligned to the target volume rather than moving the patient to align the target volume to each beam; and continual image guidance and alignment correction throughout every treatment fraction, such that there is no dependence on an absence of intrafraction motion. Motion management strategies have been developed and optimized for different applications.

(b) Minimization of the treated and irradiated volumes. This requires high dose conformality and steep dose gradients in all directions which are achieved through the combination of a robotic manipulator, which enables routine use of large numbers of non-isocentric, non-coplanar beams individually targeted at unique points within the patient without the need to reposition the patient for each beam; variable collimation, enabling multiple field sizes to be combined within each treatment such that a complex dose distribution can be constructed from a set of independently targeted and sized pencil beams; and powerful plan optimization algorithms, which select optimal beam weights, beam directions and field sizes.

Although technical developments that have led to the CyberKnife System of 2010 have enhanced its targeting and tracking accuracy, simplified treatment planning and improved the accuracy of dose calculation, and extended the applicability of the system to lesions throughout the body, these basic system requirements have been retained.

References

1. Guthrie, B. L., Adler, J. R., Jr. Computer-assisted preoperative planning, interactive surgery, and frameless stereotaxy. *Clin Neurosurg 38*, 112-131 (1992).
2. Adler, J. R., Jr., Chang S. D., Murphy M. J., Doty J., Geis P., Hancock S. L., The Cyberknife: a frameless robotic system for radiosurgery. *Stereotact Funct Neurosurg 69*, 124-128 (1997).
3. Adler, J. R., Schweikard, A., Murphy, M. J., Hancock, S. L. Image-guided cyberknife radiosurgery. In: Barnett, G., Roberts, D., Maciunas, R. J. (eds) Image-Guided Neurosurgery: Clinical Applications of Interactive Surgical Navigation, edn. Quality Medical Publishing, pp 193-204 (1998).
4. Adler, J. R., Jr., Murphy, M. J., Chang, S. D., Hancock, S. L. Image-guided robotic radiosurgery. *Neurosurgery 44*, 1299-1306; discussion 1306-1297 (1999).
5. Murphy, M. J., Cox, R. S. The accuracy of dose localization for an image-guided frameless radiosurgery system. *Med Phys 23*, 2043-2049 (1996).
6. Murphy, M. J. An automatic six-degree-of-freedom image registration algorithm for image-guided frameless stereotaxic radiosurgery. *Med Phys 24*, 857-866 (1997).
7. Schweikard, A., Bodduluri, M., Adler, J. R. Planning for camera-guided robotic radiosurgery. *IEEE Transactions on Robotics and Automation 14*, 951-962 (1998).
8. Kuo, J. S., Yu, C., Petrovich, Z., Apuzzo, M. L. The CyberKnife stereotactic radiosurgery system: description, installation, and an initial evaluation of use and functionality. *Neurosurgery 53*, 1235-1239; discussion 1239 (2003).
9. Quinn, A. M. CyberKnife: a robotic radiosurgery system. *Clin J Oncol Nurs 6*, 149, 156 (2002).
10. Antypas, C., Pantelis, E. Performance evaluation of a CyberKnife G4 image-guided robotic stereotactic radiosurgery system. *Phys Med Biol 53*, 4697-4718 (2008).
11. Sharma, S. C., Ott, J. T., Williams, J. B., Dickow, D. Commissioning and acceptance testing of a CyberKnife linear accelerator. *J Appl Clin Med Phys 8*, 2473 (2007).
12. Kilby, W., Maurer, C. R., Jr., Amies, C., Bani-Hashemi, A., Groh, B., Tuecking, T., Ruchala, K. J, Lu, W., Olivera, G. H., Mackie, T. R., Munro, P. Platforms for Image-Guided and Adaptive Radiation Therapy. In: Timmerman R, Xing L (ed) Image Guided and Adaptive Radiation Therapy, edn. Lippincott Williams and Wilkins, Philadelphia, pp 293-301 (2009).

13. Adler, J. R., Jr., Bower, R., Gupta, G., Lim, M., Efron, A., Gibbs, I. C., Chang, S. D., Soltys, S. G. Nonisocentric radiosurgical rhizotomy for trigeminal neuralgia. *Neurosurgery 64*, A84-90 (2009).

14. Colombo, F., Casentini, L., Cavedon, C., Scalchi, P., Cora, S., Francescon, P. Cyberknife radiosurgery for benign meningiomas: short-term results in 199 patients. *Neurosurgery 64*, A7-13 (2009).

15. Colombo, F., Cavedon. C., Casentini, L., Francescon, P., Causin, F., Pinna, V. Early results of CyberKnife radiosurgery for arteriovenous malformations. *J Neurosurg 111*, 807-819 (2009).

16. Soltys, S. G., Adler, J. R., Lipani, J. D., Jackson, P. S., Choi, C. Y., Puataweepong, P., White, S., Gibbs, I. C., Chang, S. D. Stereotactic radiosurgery of the postoperative resection cavity for brain metastases. *Int J Radiat Oncol Biol Phys 70*, 187-193 (2008).

17. Wowra, B., Muacevic, A., Tonn, J. C. Quality of radiosurgery for single brain metastases with respect to treatment technology: a matched-pair analysis. *J Neurooncol 94*, 69-77 (2009).

18. Dodd, R. L., Ryu, M. R., Kamnerdsupaphon, P., Gibbs, I. C., Chang, S. D., Jr., Adler, J. R., Jr. CyberKnife radiosurgery for benign intradural extramedullary spinal tumors. *Neurosurgery 58*, 674-685; discussion 674-685 (2006).

19. Gagnon, G. J., Nasr., N. M., Liao, J. J., Molzahn, I., Marsh, D., McRae, D., Henderson, F. C., Sr. Treatment of spinal tumors using cyberknife fractionated stereotactic radiosurgery: pain and quality-of-life assessment after treatment in 200 patients. *Neurosurgery 64*, 297-306; discussion 306-297 (2009).

20. Gibbs, I. C., Spinal and paraspinal lesions: the role of stereotactic body radiotherapy. *Front Radiat Ther Oncol 40*, 407-414 (2007).

21. Sahgal, A., Ames, C., Chou, D., Ma, L., Huang, K., Xu, W., Chin, C., Weinberg, V., Chuang, C., Weinstein, P., Larson, D. A. Stereotactic body radiotherapy is effective salvage therapy for patients with prior radiation of spinal metastases. *Int J Radiat Oncol Biol Phys 74*, 723-731 (2009).

22. Sinclair, J., Chang, S. D., Gibbs. I. C., Adler, J. R., Jr. Multisession CyberKnife radiosurgery for intramedullary spinal cord arteriovenous malformations. *Neurosurgery 58*, 1081-1089; discussion 1081-1089 (2006).

23. Gerszten, P. C., Burton, S. A., Ozhasoglu, C., Welch, W. C. Radiosurgery for spinal metastases: clinical experience in 500 cases from a single institution. *Spine 32,* 193-199 (2007).

24. Brown,W. T., Wu, X., Fayad, F., Fowler, J. F., Garcia, S., Monterroso, M. I., de la Zerda, A., Schwade, J. G. Application of robotic stereotactic radiotherapy to peripheral stage I non-small cell lung cancer with curative intent. *Clin Oncol (R Coll Radiol) 21*, 623-631 (2009).

25. Collins, B. T., Vahdat, S., Erickson, K., Collins, S. P., Suy, S., Yu, X., Zhang, Y., Subramaniam, D., Reichner, C. A., Sarikaya, I., Esposito, G., Yousefi, S., Jamis-Dow, C., Banovac, F., Anderson, E. D. Radical cyberknife radiosurgery with tumor tracking: an effective treatment for inoperable small peripheral stage I non-small cell lung cancer. *J Hematol Oncol 2*, 1 (2009).

26. Coon, D., Gokhale, A. S., Burton, S. A., Heron, D. E., Ozhasoglu, C., Christie, N. Fractionated stereotactic body radiation therapy in the treatment of primary, recurrent, and metastatic lung tumors: the role of positron emission tomography/computed tomography-based treatment planning. *Clin Lung Cancer 9*, 217-221 (2008).

27. van der Voort van Zyp, N. C., Prevost, J. B., Hoogeman, M. S., Praag, J., van der Holt, B., Levendag, P. C., van Klaveren, R. J., Pattynama, P., Nuyttens, J. J. Stereotactic radiotherapy with real-time tumor tracking for non-small cell lung cancer: clinical outcome. *Radiother Oncol 91*, 296-300 (2009).

28. Pennathur, A., Luketich, J. D., Heron, D. E., Schuchert, M. J., Burton, S., Abbas, G., Gooding, W. E., Ferson, P. F., Ozhasoglu, C., Gilbert, S., Landreneau, R. J., Christie, N. A. Stereotactic radiosurgery for the treatment of lung neoplasm: experience in 100 consecutive patients. *Ann Thorac Surg 88*, 1594-1600; discussion 1600 (2009).

29. Friedland, J. L., Freeman, D. E., Masterson-McGary, M. E., Spellberg, D. M. Stereotactic body radiotherapy: an emerging treatment approach for localized prostate cancer. *Technol Cancer Res Treat 8*, 387-392 (2009).

30. Fuller. D. B., Naitoh, J., Lee, C., Hardy, S., Jin, H. Virtual HDR(SM) CyberKnife Treatment for Localized Prostatic Carcinoma: Dosimetry Comparison With HDR Brachytherapy and Preliminary Clinical Observations. *Int J Radiat Oncol Biol Phys 70*, 1588-1597 (2008).

31. Katz, A. J., Santoro, M., Ashley, R., Diblasio, F., Witten, M. Stereotactic body radiotherapy for organ-confined prostate cancer. *BMC Urol 10*, 1 (2010).

32. King, C. R., Brooks, J. D., Gill, H., Pawlicki, T., Cotrutz, C., Presti, J. C., Jr. Stereotactic body radiotherapy for localized prostate cancer: interim results of a prospective phase II clinical trial. *Int J Radiat Oncol Biol Phys 73*, 1043-1048 (2009).

33. Choi, B. O., Choi, I. B., Jang, H. S., Kang, Y. N., Jang, J. S., Bae, S. H, Yoon, S. K., Chai, G. Y., Kang, K. M. Stereotactic body radiation therapy with or without transarterial chemoembolization for patients with primary hepatocellular carcinoma: preliminary analysis. *BMC Cancer 8*, 351 (2008).

34. Goodman, K. A., Wiegner, E. A., Maturen, K. E., Zhang, Z., Mo, Q., Yang, G., Gibbs, I. C., Fisher, G. A., Koong, A. C. Dose-Escalation Study of Single-Fraction Stereotactic Body Radiotherapy for Liver Malignancies. *Int J Radiat Oncol Biol Phys* (In Press).

35. Stintzing, S., Hoffmann, R. T., Heinemann, V., Kufeld, M., Muacevic, A. Frameless single-session robotic radiosurgery of liver metastases in colorectal cancer patients. *Eur J Cancer 46*, 1026-1032 (2010).

36. Hara, W., Loo, B. W., Jr., Goffinet, D. R., Chang, S. D., Adler, J. R., Pinto, H. A., Fee, W. E., Kaplan, M. J., Fischbein, N. J., Le, Q. T. Excellent local control with stereotactic radiotherapy boost after external beam radiotherapy in patients with nasopharyngeal carcinoma. *Int J Radiat Oncol Biol Phys 71*, 393-400 (2008).

37. Heron, D. E., Ferris, R. L., Karamouzis, M., Andrade, R. S., Deeb, E. L., Burton, S., Gooding, W. E., Branstetter, B. F., Mountz, J. M., Johnson, J.T., Argiris, A., Grandis, J. R., Lai, S. Y. Stereotactic body radiotherapy for recurrent squamous cell carcinoma of the head and neck: results of a phase I dose-escalation trial. *Int J Radiat Oncol Biol Phys 75*, 1493-1500 (2009).

38. Roh, K. W., Jang, J. S., Kim, M. S., Sun, D. I., Kim, B. S., Jung, S. L., Kang, J. H., Yoo, E. J., Yoon, S. C., Jang, H. S., Chung, S. M., Kim, Y. S. Fractionated stereotactic radiotherapy as reirradiation for locally recurrent head and neck cancer. *Int J Radiat Oncol Biol Phys 74*, 1348-1355 (2009).

39. Rwigema, J. C., Heron, D. E., Ferris, R. L., Gibson, M., Quinn, A., Yang, Y., Ozhasoglu, C., Burton, S. Fractionated Stereotactic Body Radiation Therapy in the Treatment of Previously-Irradiated Recurrent Head and Neck Carcinoma: Updated Report of the University of Pittsburgh Experience. *Am J Clin Oncol* (2009).

40. Teguh, D. N., Levendag, P. C., Noever, I., van Rooij, P., Voet, P., van der Est, H., Sipkema, D., Sewnaik, A., de Jong, R. B., de la Bije, D., Schmitz, P. I. Treatment Techniques and Site Considerations Regarding Dysphagia-Related Quality of Life in Cancer of the Oropharynx and Nasopharynx. *Int J Radiat Oncol Biol Phys* (2008).

41. Bondiau, P. Y., Lallement, M., Bahadoran, P., Birtwisle-Peyrottes, I., Chapellier, C., Chamorey, E., Courdi, A., Quielle-Roussel, C., Ferrero, J. M. [CyberKnife and neoadjuvant chemotherapy for breast tumors: preliminary results]. *Cancer Radiother 13*, 79-84 (2009).

42. Nuyttens, J. J., Prevost, J. B., Van der Voort van Zijp, N. C., Hoogeman, M., Levendag, P. C. Curative stereotactic robotic radiotherapy treatment for extracranial, extrapulmonary, extrahepatic, and extraspinal tumors: technique, early results, and toxicity. *Technol Cancer Res Treat 6*, 605-610 (2007).

43. Echner, G. G., Kilby, W., Lee, M., Earnst, E., Sayeh, S., Schlaefer, A., Rhein, B., Dooley, J. R., Lang, C., Blanck, O., Lessard, E., Maurer, C. R., Jr., Schlegel, W. The design, physical properties and

clinical utility of an iris collimator for robotic radiosurgery. *Phys Med Biol 54*, 5359-5380 (2009).

44. Alfonso, R., Andreo, P., Capote, R., Huq, M. S., Kilby,W., Kjall, P., Mackie, T. R., Palmans, H., Rosse, K., Seuntjens, J., Ullrich, W., Vatnitsky, S. A new formalism for reference dosimetry of small and nonstandard fields. *Med Phys 35*, 5179-5186 (2008).

45. Pantelis, E., Moutsatsos, A., Zourari, K., Kilby, W., Antypas, C., Papagiannis, P., Karaiskos, P., Georgiou, E., Sakelliou, L. On the implementation of a recently proposed dosimetric formalism to a robotic radiosurgery system. *Med Phys 37*, 2369-2379 (2010).

46. Fu, D., Kuduvalli, G. A fast, accurate, and automatic 2D-3D image registration for image-guided cranial radiosurgery. *Med Phys 35*, 2180-2194 (2008).

47. Fu, D., Kuduvalli, G. Enhancing Skeletal Features in Digitally Reconstructed Radiographs. *Proc SPIE 6144*, 846-851 (2006).

48. Fu, D., Kuduvalli, G., Maurer, C. R., Jr., Allison, J. W., Adler, J. R., Jr. 3D target localization using 2D local displacements of skeletal structures in orthogonal x-ray images for image-guided spinal radiosurgery. *Int J Comput Assist Radiol Surg 1*, 198-200 (2006).

49. Ho, A. K., Fu, D., Cotrutz, C., Hancock, S. L., Chang, S. D., Gibbs, I. C., Maurer, C. R, Jr., Adler, J. R., Jr. A study of the accuracy of Cyberknife spinal radiosurgery using skeletal structure tracking. *Neurosurgery 60*, 147-156 (2007).

50. Jordan, P., West, J. B., Sharda, A., Maurer, C. R., Jr. Retrospective Clinical Data Analysis of Fiducial-Free Lung Tracking. *Med Phys 37*, 3150 (2010).

51. Fu, D., Kahn, R., Wang, B., Wang, H., Mu, Z., Park, J., Kuduvalli, G., Maurer, C. R, Jr. Xsight Lung Tracking System: A fiducial-less method for respiratory motion tracking. In: Urschel, H. C., Jr, Kresl, J. J., Luketich, J. D., Papiez, L., Timmerman, R. D. (ed) Robotic Radiosurgery: Treating Tumors that Move with Respiration, edn. Springer-Verlag, Berlin, pp 265-282 (2007).

52. Anantham, D., Feller-Kopman, D., Shanmugham, L. N., Berman, S. M., Decamp, M. M., Gangadharan, S. P., Eberhardt, R., Herth, F., Ernst, A. Electromagnetic navigation bronchoscopy guided fiducial placement for robotic stereotactic radiosurgery of lung tumors — a feasibility study. *Chest* (2007).

53. Reichner, C. A., Collins, B. T., Gagnon, G. J., Malik, S., Jamis-Dow, C., Anderson, E. D. The placement of gold fiducials for CyberKnife stereotactic radiosurgery using a modified transbronchial needle aspiration technique. *Journal of Bronchology 12*, 193-195 (2005).

54. Mu, Z., Fu, D., Kuduvalli, G. Multiple fiducial identification using the hidden Markov model in image guided radiosurgery In: Computer Vision and Pattern Recognitio IEEE Computer Society. Washington, DC (2006).

55. Hatipoglu, S., Mu, Z., Fu, D., Kuduvalli, G. Evaluation of a robust fiducial tracking algorithm for image-guided radiosurgery. *Proc SPIE 6509*, 65090A (2007).

56. Mu, Z., Fu, D., Kuduvalli, G. A probabilistic framework based on hidden Markov model for fiducial identification in image-guided radiation treatments. *IEEE Trans. Med. Imaging 27*, 1288-1300 (2008).

57. Schweikard, A., Shiomi, H., Adler, J. Respiration tracking in radiosurgery. *Med Phys 31*, 2738-2741 (2004).

58. Sayeh, S., Wang, J., Main, W. T., Kilby, W., Maurer, C. R., Jr. Respiratory motion tracking for robotic radiosurgery. In: Urschel, H. C., Jr., Kresl, J. J., Luketich, J. D., Papiez, L., Timmerman, R. D. (ed) Robotic Radiosurgery: Treating Tumors that Move with Respiration, edn. Springer-Verlag, Berlin, pp 15-29 (2007).

59. Keall, P. J., Mageras, G. S., Balter, J. M., Emery, R. S., Forster, K. M., Jian, S. B., Kapatoes, J. M., Low, D. A., Murphy, M. J., Murray, B. R., Ramsey, C. R., van Herk, M. B., Vedam, S. S., Wong, J. W., Yorke, E. The management of respiratory motion in radiation oncology. *Med Phys 44*, 3874-3900 (2006).

60. Seppenwoolde, Y., Berbeco, R. I., Nishioka, S., Shirato, H., Heijmen, B. Accuracy of tumor motion compensation algorithm from a robotic

respiratory tracking system: a simulation study. *Med Phys 34*, 2774-2784 (2007).

61. Shirato, H., Seppenwoolde, Y., Kitamura, K., Onimura, R., Shimizu, S. Intrafractional tumor motion: Lung and liver. *Semin Radiat Oncol 14*, 10-18 (2004).

62. Maurer, C. R., Jr., West, J. B. Medical image registration using mutual information. In: Heilbrun, M. P. (ed) CyberKnife Radiosurgery: Practical Guide 2, edn. The CyberKnife Society, Sunnyvale, CA (2006).

63. Studholme, C., Hill, D. L., Hawkes, D. J. Automated 3-D registration of MR and CT images of the head. *Med Image Anal 1*, 163-175 (1996).

64. Ma, C.-M., Li, J. S., Deng, J., Fan, J. Implementation of Monte Carlo dose calculation for CyberKnife treatment planning. *J Phys: Conf Ser 102*, 012016 (2008).

65. Hol, M., Marijnissen, J. P. A., van der Baan, P., Heijmen, B. J. M. Accuracy of the Monte Carlo dose calculation algorithm for CyberKnife treatment of small lung lesions. *Med Phys* 35, 2953 (2008).

66. Muniruzzaman, M., Dooley, J., Kilby, W., Lee, M.Y., Maurer, C. R., Jr., Sims, C. Validation tests for CyberKnife® Monte Carlo dose calculations using heterogeneous phantoms. *Med Phys* 35, 2953 (2008).

67. Wilcox, E. E., Daskalov, G. M. Accuracy of dose measurements and calculations within and beyond heterogeneous tissues for 6 MV photon fields smaller than 4 cm produced by Cyberknife. *Med Phys 35*, 2259-2266 (2008).

68. Sharma, S. C., Ott, J. T., Williams, J. B., Dickow, D. Clinical implications of adopting Monte Carlo treatment planning for CyberKnife. *J Appl Clin Med Phys 11*, 3142 (2010).

69. van der Voort van Zyp, N. C., Hoogeman, M., Heijmen, B., Levendag, P., van der Holt, B., van de Water, S., Nuyttens, J. Clinical introduction of Monte Carlo treatment planning; a different prescription dose for non-small cell lung cancer according to tumor location and size. *Radiat Oncol 96*, 55-60 (2010).

70. Schlaefer, A., Schweikard, A. Stepwise multi-criteria optimization for robotic radiosurgery. *Med Phys 35*, 2094-2103 (2008).

71. Lessard, E., Kilby, W., Dooley, J., Sims, C., Schlaefer, A., Blanck, O., Maurer, C. R., Jr. Sequential optimization scripts to facilitate treatment planning for robotic radiosurgery clinical studies for prostate and lung cancers In: World Congress on Medical Physics and Biomedical Engineering. Munich, Germany. pp 1031-1034 (2009).

72. Maciunas, R. J., Galloway, R. L., Jr., Latimer, J. W. The application accuracy of stereotactic frames. *Neurosurgery* 35, 682-694; discussion 694-685 (1994).

73. Chang, S. D., Main, W., Martin, D. P., Gibbs, I. C., Heilbrun, M. P. An analysis of the accuracy of the CyberKnife: a robotic frameless stereotactic radiosurgical system. *Neurosurgery 52*, 140-146; discussion 146-147 (2003).

74. Main, W. T., Adler, J. R., Bodduluri, M., Core, M., Taylor, D. CyberKnife Targeting Accuracy Using the CK-6 Algorithm. In.: Accuray, Inc.; 2003.

75. Murphy, M. J. Fiducial-based targeting accuracy for external-beam radiotherapy. *Med Phys 29*, 334-344 (2002).

76. Hoogeman, M. S., Nuyttens, J. J., Levendag, P. C., Heijmen, B. J. Time dependence of intrafraction patient motion assessed by repeat stereoscopic imaging. *Int J Radiat Oncol Biol Phys 70*, 609-618 (2008).

77. Murphy, M. J. Intrafraction geometric uncertainties in frameless image-guided radiosurgery. *Int J Radiat Oncol Biol Phys 73*, 1364-1368 (2009).

78. van Herk, M., Remeijer, P., Lebesque, J. V. Inclusion of geometric uncertainties in treatment plan evaluation. *Int J Radiat Oncol Biol Phys 52*, 1407-1422 (2002).

79. Fürweger, C., Drexler, C., Kufeld, M., Muacevic, A., Wowra, B., Schlaefer, A. Patient Motion and Targeting Accuracy in Robotic Spinal Radiosurgery: 260 Single-Fraction Fiducial-Free Cases. *Int J Radiat Oncol Biol Phys* (In press).

80. Chuang, C., Sahgal, A., Lee, L., Larson, D., Huang, K., Petti, P., Verhey, L., Ma, L. Effects of residual target motion for image-tracked spine radiosurgery. *Med Phys 34*, 4484-4490 (2007).

81. Kupelian, P., Willoughby, T., Mahadevan, A., Djemil, T., Weinstein, G., Jani, S., Enke, C., Solberg, T., Flores, N., Liu, D., Beyer, D., Levine, L. Multi-institutional clinical experience with the Calypso System in localization and continuous, real-time monitoring of the prostate gland during external radiotherapy. *Int J Radiat Oncol Biol Phys 67*, 1088-1098 (2007).

82. Xie, Y., Djajaputra, D., King, C. R., Hossain, S., Ma, L., Xing, L. Intrafractional motion of the prostate during hypofractionated radiotherapy. *Int J Radiat Oncol Biol Phys 72*, 236-246 (2008).

83. Seppenwoolde, Y., Shirato, H., Kitamura, K., Shimizu, S., van Herk, M., Lebesque, J. V., Miyasaka, K. Precise and real-time measurement of 3D tumor motion in lung due to breathing and heartbeat, measured during radiotherapy. *Int J Radiat Oncol Biol Phys 53*, 822-834 (2002).

84. Dieterich, S., Taylor, D., Chuang, C., Wong, K., Tang, J., Kilby, W., Main, W. The CyberKnife Synchrony Respiratory Tracking System: Evaluation of systematic targeting uncertainty [white paper]. Sunnyvale, CA: Accuray, Incorporated (2004).

85. Cavedon, C., Chuang, C., Dieterich, S., Drexler, C., Taylor, D., Wu, X. A multi-institutional validation of Synchrony motion tracking accuracy using the Accuray Synchrony quality assurance motion generation tool – A work in progress In: 6th Annual CyberKnife Users' Meeting CyberKnife Society. Sunnyvale, CA (2007).

86. Muacevic, A., Staehler, M., Drexler, C., Wowra, B., Reiser, M., Tonn, J. C. Technical description, phantom accuracy, and clinical feasibility for fiducial-free frameless real-time image-guided spinal radiosurgery. *J Neurosurg Spine 5*, 303-312 (2006).

87. Main, W., Taylor, D., Hatipoglu, S., Sayeh, S., Kilby, W., Maurer, C. R., Jr. The CyberKnife Synchrony Respiratory Tracking System: Initial Evaluation of Nonlinear Correlation Model [white paper]. Sunnyvale, CA: Accuray, Incorporated (2005).

88. Kilby, W., Main, W. M., Dieterich, S., Taylor, D., Wu, X. In-vivo assessment of the Synchrony Respiratory Tracking System accuracy In: 5th Annual CyberKnife Users' Meeting CyberKnife Society. Sunnyvale, CA (2006).

89. Hoogeman, M., Prevost, J. B., Nuyttens, J., Poll, J., Levendag, P., Heijmen, B. Clinical accuracy of the respiratory tumor tracking system of the cyberknife: assessment by analysis of log files. *Int J Radiat Oncol Biol Phys 74*, 297-303 (2009).

90. Sheng, Y., Shutian, L., Sayeh, S., Wang, J., Wang, H. Fuzzy and Hybrid Prediction of Position Signal in Synchrony® Respiratory Tracking System In: Ninth IASTED International Conference, Signal and Image Processing. Honolulu, HI (2007).

91. Berbeco, R. I., Nishioka, S., Shirato, H., Chen, G. T., Jiang, S. B. Residual motion of lung tumours in gated radiotherapy with external respiratory surrogates. *Phys Med Biol 50*, 3655-3667 (2005).

92. Nioutsikou, E., Seppenwoolde, Y., Symonds-Tayler, J. R., Heijmen, B., Evans, P., Webb, S. Dosimetric investigation of lung tumor motion compensation with a robotic respiratory tracking system: an experimental study. *Med Phys 35*, 1232-1240 (2008).

93. Wong, K. H., Dieterich, S., Tang, J., Cleary, K. Quantitative Measurement of CyberKnife Robotic Arm Steering. *Technol Cancer Res Treat 6*, 589-594 (2007).

94. Adler, J. R., Cox, R. S. Preliminary clinical experience with the CyberKnife: image-guided stereotactic radiosurgery. In: Alexander E., III, Kondziolka, D., Loeffler, J. S. (ed) Radiosurgery 1995, edn. Karger, Basel, Switzerland, pp 316-326 (1996).

95. Ryu, S. I., Chang, S. D., Kim, D. H., Murphy, M. J., Le, Q. T., Martin, D. P., Adler, J. R., Jr. Image-guided hypo-fractionated stereotactic radiosurgery to spinal lesions. *Neurosurgery 49*, 838-846 (2001).

96. King, C. R., Lehmann, J., Adler, J. R., Hai, J. CyberKnife radiotherapy for localized prostate cancer: rationale and technical feasibility. *Technol Cancer Res Treat 2*, 25-30 (2003).

97. Koong, A. C., Le, Q. T., Ho, A., Fong, B., Fisher, G., Cho, C., Ford, J., Poen, J., Gibbs, I. C., Mehta, V. K., Kee, S., Trueblood, W., Yang, G., Bastidas, J. A. Phase I study of stereotactic radiosurgery in patients with locally advanced pancreatic cancer. *Int J Radiat Oncol Biol Phys 58*, 1017-1021 (2004).

98. Whyte, R. I., Crownover, R., Murphy, M. J., Martin, D. P., Rice, T. W., DeCamp, M. M., Jr., Rodebaugh, R., Weinhous, M. S., Le, Q. T. Stereotactic radiosurgery for lung tumors: preliminary report of a phase I trial. *Ann Thorac Surg 75*, 1097-1101 (2003).

99. Chang, D. T., Schellenberg, D., Shen, J., Kim, J., Goodman, K. A., Fisher, G. A., Ford, J. M., Desser, T., Quon, A., Koong, A. C. Stereotactic radiotherapy for unresectable adenocarcinoma of the pancreas. *Cancer 115*, 665-672 (2009).

100. Mahadevan, A., Jain, S., Goldstein, M., Miksad, R., Pleskow, D., Sawhney, M., Brennan, D., Callery, M., Vollmer, C. Stereotactic Body Radiotherapy and Gemcitabine for Locally Advanced Pancreatic Cancer. *Int J Radiat Oncol Biol Phys* (In Press).

101. Yu, C., Main, W., Taylor, D., Kuduvalli, G., Apuzzo, M. L., Adler, J. R., Jr. An anthropomorphic phantom study of the accuracy of Cyberknife spinal radiosurgery. *Neurosurgery 55*, 1138-1149 (2004).

102. Muacevic, A., Drexler, C., Wowra, B., Schweikard, A., Schlaefer, A., Hoffmann, R. T., Wilkowski, R., Winter, H., Reiser, M. Technical Description, Phantom Accuracy, and Clinical Feasibility for Single-session Lung Radiosurgery Using Robotic Image-guided Real-time Respiratory Tumor Tracking. *Technol Cancer Res Treat 6*, 321-328 (2007).